Advances in Geo-Energy Research

Vol. 6, No. 1, p. 23-37, 2022

Original article

Strengthening and weakening of methane hydrate by water vacancies

Yanwen Lin[1,2], Yisi Liu[1], Ke Xu[1], Tong Li[2]*, Zhisen Zhang[1], Jianyang Wu[1,3]*

[1]*Department of Physics, Research Institute for Biomimetics and Soft Matter, Jiujiang Research Institute and Fujian Provincial Key Laboratory for Soft Functional Materials Research, Xiamen University, Xiamen 361005, P. R. China*

[2]*Key Laboratory of Marine Materials and Related Technologies, Zhejiang Key Laboratory of Marine Materials and Protective Technologies, Ningbo Institute of Materials Technology and Engineering, Chinese Academy of Sciences, Ningbo 315201, P. R. China*

[3]*NTNU Nanomechanical Lab, Norwegian University of Science and Technology (NTNU), Trondheim 7491, Norway*

Keywords:
Methane hydrates
water vacancy
structural properties
mechanical properties
molecular dynamics simulations

Cited as:
Lin, Y., Liu, Y., Xu, K., Li, T., Zhang, Z., Wu, J. Strengthening and weakening of methane hydrate by water vacancies. Advances in Geo-Energy Research, 2022, 6(1): 23-37.
https://doi.org/10.46690/ager.2022.01.03

Abstract:
Gas clathrate hydrates show promising applications in sustainable technologies such as future energy resources, gas capture and storage. The stability of clathrate hydrates under external load is of great crucial to those important applications, but remains unknown. Water vacancy is a common structural defect in clathrate hydrates. Herein, the mechanical characteristics of sI methane hydrates containing three types of water vacancy are investigated by molecular dynamics simulations with four different water forcefields. Mechanical properties of methane hydrates such as tensile strength are dictated not only by the density but also the type of water vacancy. Surprisingly, the tensile strength of methane hydrates can be weakened or strengthened, depending on the adopted water model and water vacancy density. Strength enhancement mainly results from the formation of new water cages. This work provides critical insights into the mechanics and microstructural properties of methane clathrate hydrates under external load, which is of primary importance in the recovery of natural gas from methane hydrate reservoirs.

1. Introduction

Natural gas hydrates (NGHs) are ice-like crystalline solids composed of water molecular cages that encapsulate methane molecules. As is known, NGHs occur in the seabed and underground permafrost sediments at conditions of high pressures and low temperatures (Koh and Sloan, 2007; Chong et al., 2016; Hansen et al., 2016). The cubic structural I clathrate hydrates is the most common NGH structure in natural setting environments (Udachin et al., 2001; Sloan, 2003). NGHs possess a high capacity to store natural gas (mainly methane molecules), that is, one cubic meter of NGHs contains approximately 180 standard cubic meters of methane gas at conditions of room temperature and standard pressure (Rempel and Buffett, 1997; Shaibu et al., 2021). To date, it is conservatively estimated that the amount of energy resource stored in gas hydrates is around 2-folds of that in conventional fossil fuels (Walsh et al., 2009). Recently, because of the huge reserves in nature and eco-friendly properties, NGHs are increasingly recognized as alternative fuel resources (Everett et al., 2013, 2015; Chen et al., 2015; Shaibu et al., 2021), thereby the recovery of natural gas from NGHs has attracted great attention (Uchida et al., 2004; Waite et al., 2009; Ning et al., 2012; Liu et al., 2013; Casco et al., 2015; Fan et al., 2017).

The mechanical behaviors of NGHs are of importance for assessing the mechanical stability of NGHs-bearing sediments and for improving the commercial exploiting technology of NGHs and hydrates-related applications (Luff and Wallmann, 2003; Graves et al., 2017). As a result, a number of investigations on the mechanical properties of clathrate hydrates have been experimentally and theoretically conducted (Jendi et al.,

Yandy Scientific Press

*Corresponding author.
E-mail address: linyanwenfn@163.com (Y. Lin); liu54614@foxmail.com (Y. Liu); twtdq@stu.xmu.edu.cn (K. Xu); tong@nimte.ac.cn (T. Li); zhangzs@xmu.edu.cn (Z. Zhang); jianyang@xmu.edu.cn (J. Wu).

Received December 3, 2021; revised December 22, 2021; accepted December 23, 2021; available online December 27, 2021.

2015; Wu et al., 2015; Shi et al., 2018; Atig et al., 2020; Cao et al., 2020; Xu et al., 2020; Cao et al., 2021). By using a novel contactless thermal method to impose loading stress, the tensile elastic modulus and strength of methane hydrates were estimated, and, depending on the sample thickness and texture, ductile and brittle characteristics were both found via the video microscopy to observe the strain (Atig et al., 2020). Using molecular dynamics (MD) simulations, the effects of engineering strain rate, temperature, crystal orientation, guest molecules, cage occupancy and nanovoids on the mechanical properties of clathrate hydrates were examined (Wu et al., 2015; Cao et al., 2020; Xu et al., 2020). It was revealed that the fundamental mechanical properties such as tensile strength limit, fracture strain and destabilization pattern are dominated by the guest molecular property such as size, shape and polarity (Shi et al., 2018; Xin et al., 2021). Moreover, the degree of occupancy of guest molecules in the large $5^{12}6^2$ cages primarily determines the mechanical strength and elastic limit of clathrate hydrates (Cao et al., 2018).

In reality, water cages-dominated crystalline clathrate hydrates in natural settings and laboratories are imperfect crystals, and inevitably contain defects including water vacancies, interstitial defects and grain boundaries (Roman-Perez et al., 2010; Vidal-Vidal et al., 2015, 2016; Liang et al., 2016). Similar to other solid crystals, the properties of crystalline clathrate hydrates could be greatly influenced by those defects (Wu et al., 2015; Liang et al., 2016, 2017; Lo et al., 2017; Cao et al., 2020, 2021). For example, it was revealed that water vacancy defects in clathrate hydrates promote the local hopping and diffusion behaviors of guest molecules across clathrate cages (Liang et al., 2016). A single water vacancy defect could result in the damage of four clathrate cages on average, as well as that the damage of clathrate cages propagates in the clathrate hydrate systems (Lo et al., 2017). By increasing the density of water vacancy defect, isolated damaged cages in clathrate hydrate by single defect aggregate once they interfere with each other (Lo et al., 2017). Mechanically, it was found that the defects of grain boundaries play significant roles in the mechanical characteristics of methane hydrate polycrystals (Wu et al., 2015, 2017; Cao et al., 2020, 2021; Sveinsson et al., 2021), for example, sI methane hydrates containing networked grain boundaries shows abnormous strength with increasing grain size (Wu et al., 2015, 2017; Cao et al., 2020). Despite the abovementioned important progress in the study of the properties of clathrate hydrates containing defects, how water vacancy defects affect their mechanical characteristics remains unknown yet.

To this end, this study aims to reveal the role of water vacancies on the mechanical properties of sI methane hydrates subjected to a load, as well as the microstructural properties, particularly for the strain-induced dissociation and structural transformation of clathrate cages. Using classic MD simulations with four different water forcefields including TIP4P, TIP4P/2005, TIP4P/ICE and TIP4P/EW, the tensile mechanical characteristics of methane hydrates with three distinct positional water vacancies and different density of water vacancy subjected to uniaxial load are comprehensively contrasted. The fundamental structural and mechanical properties such as lattice constant, tensile strength and failure mechanisms of perfect and defective sI methane hydrates are investigated. Moreover, the dynamics such as geometrical sphericity and structural transformations of clathrate cages in methane hydrate systems subjected to mechanical load are analyzed.

2. Models and methods

2.1 Methane clathrate hydrate structure

As is known, the structural I methane hydrate is the most common clathrate hydrate identified in nature, thereby it is taken into an investigation in this study (Cai et al., 2019). For construction of the molecular model of sI methane hydrate, the positions of water oxygen atoms are attained from X-ray diffraction experimental data by McMullan et al. (1965) Hydrogen atoms are initially covalently-bonded to the oxygen atoms in random directions, while the positions of hydrogen atoms are further determined based on the Bernal-Fowler rule, ensuring that the total dipole moment of water molecules is small. Guest methane molecules are placed at the center of clathrate cage with random molecular orientations. The initial lattice constant of sI methane hydrate is approximately 12.0 Å. In this study, supercell of $3 \times 3 \times 3$ unit cells of sI methane hydrate structure that is composed of 1242 water molecules and 216 methane molecules is created, as illustrated in Fig. 1.

To generate methane hydrate containing water vacancies, water molecules are directly removed. Note that, for sI methane hydrate with Pm3n space group, the 46 host water molecules in the unit cell are classified into three types on the basis of spatial water positions in the lattice, and of which there are 6, 16 and 24 water molecules, respectively. As illustrated by Fig. 1(d), those three types of host water molecules in sI clathrate hydrates are blue-, red- and green-painted for clarification. To be rigorous in revealing the effects of defects on the mechanical properties, seven molecular models of sI methane hydrates with different defects of water vacancy, marked as M0-7, are constructed. For example, mark of M4-7 denotes multiple water vacancies that are located at different positions. More information is listed in Table 1. Periodic boundary conditions are applied in all three directions of the simulation box.

2.2 MD simulations

The host water molecules in the sI clathrate hydrates are mimicked by four water models including TIP4P, TIP4P/2005, TIP4P/ICE, and TIP4P/EW (Abascal and Vega, 2005; Jacobson and Molinero, 2010), while the guest methane molecules are modeled by OPLS-AA forcefield (Kaminski et al., 1994; Jorgensen et al., 1996). Based on those forcefields, the MD results by the four water models can be compared. The intermolecular nonbonded interactions (U_{ij}) in the clathrate hydrate systems are described by the standard 12-6 Lennard-Jones (L-J) potential as follow

$$U_{ij} = 4\varepsilon_{ij}\left[\left(\frac{\sigma_{ij}}{r_{ij}}\right)^{12} - \left(\frac{\sigma_{ij}}{r_{ij}}\right)^{6}\right] + \frac{q_i q_j}{4\pi\varepsilon_0 r_{ij}} \quad (1)$$

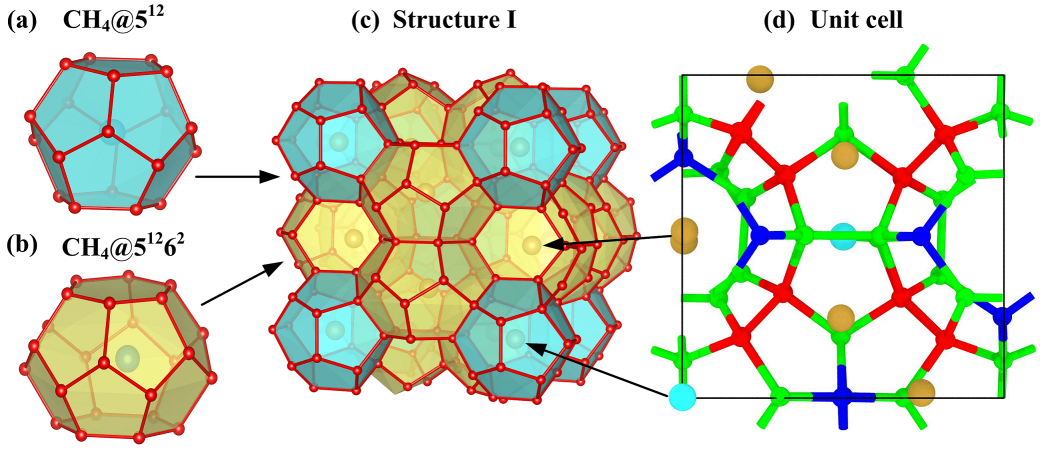

Fig. 1. Molecular structure of sI methane hydrates. (a) Water molecular cages of $CH_4@5^{12}$composed of 12 pentagonal faces, (b) $CH_4@5^{12}6^2$ composed of 12 pentagonal and two hexagonal faces, and (c) the sI crystal structure of methane hydrate. (d) The unit cell of methane hydrate, in which the methane molecules are placed at random orientations in the center of each cage, and 46 water molecules are divided into three categories. The number of water molecules in each category is 6, 16, and 24, respectively, which are displayed in blue, red and green colors.

Table 1. The models of sI methane hydrates with various water vacancy defects.

Models	Type of water defects	Molecular number	
		H_2O	CH_4
M0	Defect-free	1242	216
M1	O6/Type I	1241	216
M2	O16/Type II	1241	216
M3	O24/Type III	1241	216
M4	O16-O6	1240	216
M5	O24-O6	1240	216
M6	O24-O16	1240	216
M7	O24-O16-O6	1239	216

where r_{ij} is the distance between two particles i and j, while ε_{ij} and σ_{ij} are the energy and size parameter for the L-J 12-6 interactions, respectively. q_i and q_j are the point charge particles i and j, respectively. ε_0 is the dielectric constant of atoms. The combining rules of Lorentz-Berthelot are adopted in the interaction parameters between unlike L-J pairs. For the L-J interactions, the cutoff distance is assigned to be 12.0 Å that is around one-third of the edge length of the simulation box, whereas for the long-range electrostatic contributions, the particle-particle particle-mesh method is utilized.

Prior to MD runs, the initial configurations of sI methane hydrates are structurally optimized with energy and force tolerances of 1.0×10^{-10} Kcal/mol and 1.0×10^{-10} Kcal/(mol·Å), respectively. Then, simulations with 2 ns are ran to fully relax as-optimized hydrate system at 253.15 K and confining pressure of 100 bar under the constant number of particles, constant pressure, and constant temperature (NPT) ensemble. The temperature and confining pressure are maintained by the Nosé-Hoover thermostat and Nosé-Hoover barostat methods with damping times of 0.1 and 1 ps, respectively. The velocities of water and guest molecules in the hydrate system follow Gaussian distribution on the basis of the given temperature. The Velocity-Verlet integration method with a timestep of 1 fs is employed to integrate Newton's motion for the hydrate systems. The deformation control technique is adopted to impose uniaxial load on the hydrate samples under NPT ensemble, and a constant engineering straining rate of 10^8/s is adopted. During the uniaxial tension simulations, the lateral pressure of samples is independently controlled, allowing lateral expansion/contraction due to Poisson effect. All the simulations are implemented using the Large-Scale Atomic-Molecular Massively Parallel Simulator software package (Plimpton, 1995).

3. Results and discussion

3.1 Formation energy of water vacancy

Vacancy is the simplest and common form of defect in crystals, and it alters many physical and mechanical properties of crystals in various ways. The formation energy of water vacancy is one of the important properties of crystalline clathrate hydrates, and it represents the energy required to break the hydrogen bonds between one water molecule inside the lattice and its nearest neighbor water molecules and remove that water molecule to where no interactions between it and the remaining molecules exist. Similar to the oxygen vacancy formation energy in perovskites (Lee et al., 2009; Mayeshiba and Morgan, 2017), the formation energy of water vacancy (E_{vf}) in the crystalline clathrate hydrates is determined as follows

$$E_{vf} = E_d - E_u + E_0 \tag{2}$$

where E_d and E_u are the total energies of water vacancy-contained and -free clathrate hydrate systems, respectively, and E_0 is the potential energy of single water molecule in

vacuum environment. Table 2 lists the formation energy of water vacancy of the M1-3 models predicted by the TIP4P, TIP4P/2005, TIP4P/ICE, and TIP4P/EW water forcefields. Apparently, the formation energy of vacancy of one water molecule in sI methane hydrate crystal depends on the position of water vacancy and water forcefield. For example, E_{vf} of the M1 model varies from around 0.47-0.64 eV, depending on the applied water forcefield, with the maximum and minimum values for TIP4P/ICE and TIP4P forcefields. For the case of the M2 and 3 models, E_{vf} varies from 0.42/0.35-0.54/0.59 eV, with the maximum and minimum values for TIP4P/ICE/TIP4P/EW and TIP4P/2005/TIP4P forcefields, respectively. Previous studies (de Koning et al., 2006; Watkins et al., 2011) revealed that the formation energy of one water vacancy in crystalline hexagon water ice varies from around 0.68-0.74 eV, depending on the calculation techniques of Density Functional Theory. By comparison, sI methane hydrate crystal shows lower formation energy of one water molecule vacancy than hexagonal water ice crystal, indicating that water molecule vacancies occur more easily in sI methane hydrates than that in hexagonal water ice crystal.

3.2 Lattice parameter of sI methane hydrate with defects of water vacancy

Figs. 2(a)-2(c) shows the edge lengths of equilibrated M0-7 models of one unit-cell sI methane hydrate in the three orthogonal (x, y and z) directions by using TIP4P, TIP4P/2005, TIP4P/ICE, and TIP4P/EW water forcefields. It is observed that there is a slight reduction by the concentration and location of water vacancy in the edge lengths of sI methane hydrate. However, there are apparent differences in the edge lengths predicted by the four water forcefields. Moreover, for a given water forcefield, there are differences between three edge lengths, indicating that defects of water vacancy cause different structural deformations in the three orthogonal directions. Fig. 2(d) shows the average edge length of equilibrated M0-7 models of one unit-cell sI methane hydrate predicted by TIP4P, TIP4P/2005, TIP4P/ICE, and TIP4P/EW water forcefields. The predicted average edge length represents the lattice constant of sI methane hydrate. Obviously, the lattice constant of sI methane hydrate depends on the utilized water forcefields, and in terms of the value of the predicted lattice constant, a ranking order as TIP4P/ICE >TIP4P/2005 >TIP4P/EW >TIP4P can be observed. Previous studies also showed that the TIP4P/ICE water model produces larger lattice constant in comparison with other water models (Costandy et al., 2016). Moreover, those MD simulation results of lattice constant of sI methane hydrate are in good agreement with the experimental data reported by Shpakov et al. (1998) and Ogienko et al. (2006).

3.3 Mechanical properties of defective sI methane hydrates

Figs. 3(a)-3(d) shows the tensile stress-strain curves of defect-free and water vacancy defect-contained sI methane hydrates under uniaxial tension predicted by TIP4P, TIP4P/2005,

Table 2. Formation energy of water vacancy of the M1-3 models that represent three types of defects in sI methane hydrates.

Property	Forcefield	M1	M2	M3
Vacancy energy (eV)	TIP4P	0.47 ± 0.258	0.51 ± 0.252	0.35 ± 0.259
	TIP4P/2005	0.50 ± 0.263	0.42 ± 0.240	0.45 ± 0.253
	TIP4P/ICE	0.64 ± 0.255	0.54 ± 0.252	0.57 ± 0.230
	TIP4P/EW	0.49 ± 0.256	0.48 ± 0.257	0.59 ± 0.273

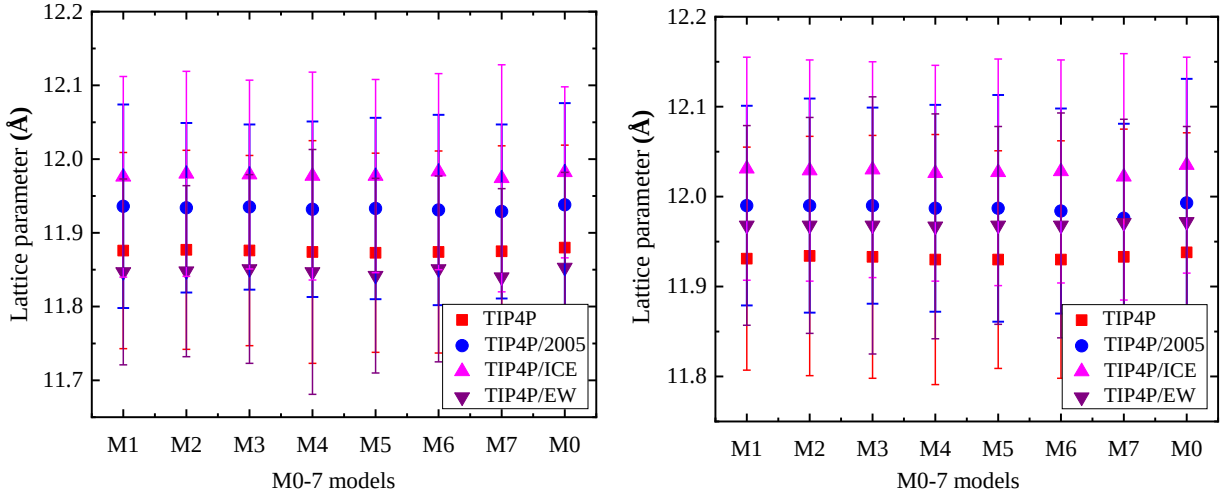

(a) X direction (b) Y direction

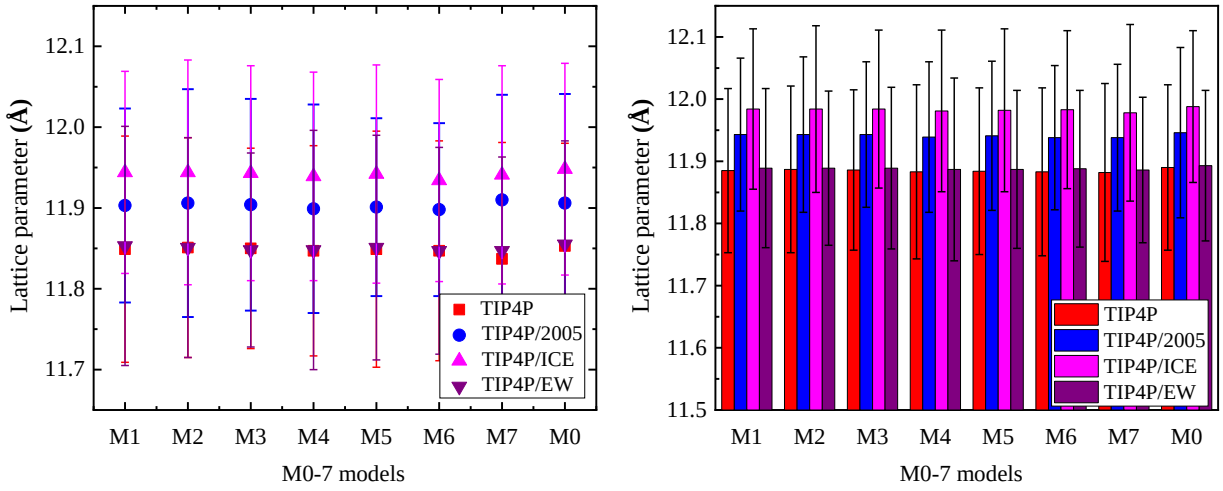

(c) Z direction (d) The average of three directions

Fig. 2. Lattice constants of the M0-7 models obtained by different water models after NPT relaxation.

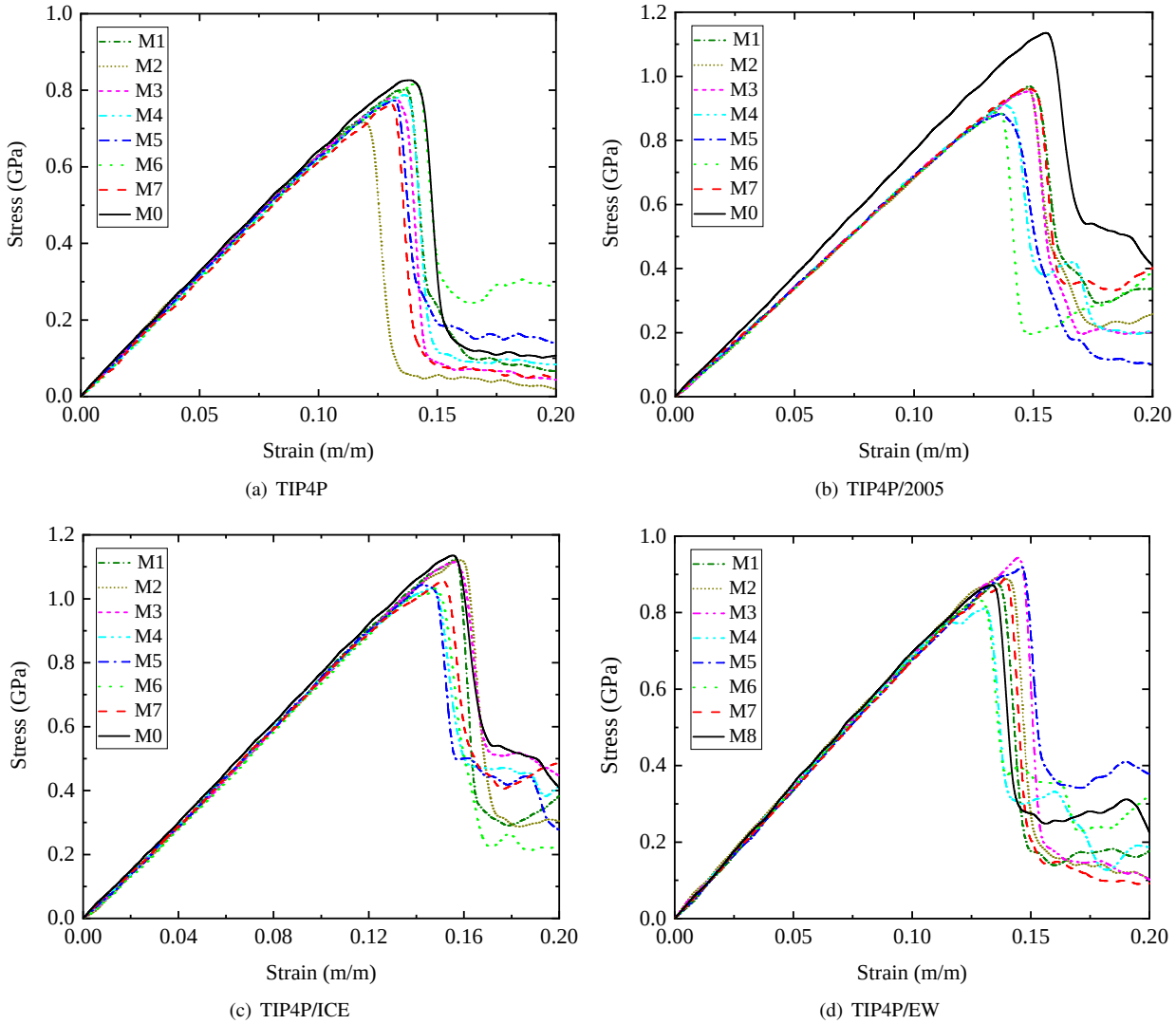

(a) TIP4P (b) TIP4P/2005

(c) TIP4P/ICE (d) TIP4P/EW

Fig. 3. Tensile stress-strain curves of M0-7 models obtained under the four popular water models.

Table 3. Ultimate tensile strengths of sI methane hydrates containing a variety of vacancy defects.

Property	Forcefield	M1	M2	M3	M4	M5	M6	M7	M0
Tensile strength (GPa)	TIP4P	0.802	0.716	0.781	0.788	0.773	0.818	0.764	0.826
	TIP4P/2005	0.970	0.962	0.954	0.911	0.884	0.892	0.963	1.135
	TIP4P/ICE	1.124	1.122	1.114	1.034	1.044	1.032	1.055	1.135
	TIP4P/EW	0.877	0.893	0.943	0.811	0.920	0.832	0.887	0.872

TIP4P/ICE, and TIP4P/EW water forcefields. It should be noted that water vacancy defect-contained samples are generated by raondom removal of water molecule/molecules in the M0 model to produce different M1-7 models. The stress response curves predicted by the four popular water models can be roughly classified into three stages for all tested samples. Stage I corresponds to the initial linearity in the loading stress-strain curve, indicating that methane hydrate is linearly-elastic deformed subjected to initial tension. Stage II is characterized by the nonlinear stress-strain curves, that is, the increase in the tensile stress mainly becomes less significant with increasing strain. This is indicative of strain-induced softening behaviors. By comparing, there are negligible differences in the elastic responses of various defective sI methane hydrates for one given water forcefield. Interestingly, when approaching the final loading of stage II predicted by the TIP4P/EW water model, oscillation-like changes in the tensile stress with strain are uniquely identified, indicating distinct yielding of hydrate samples from that predicted by other water models. In the final stage, it is observed sudden deep drop of loading stress at critical strains, suggesting the strain-induced failure of hydrate samples.

The mechanical properties of hydrate samples can be characterized by ultimate tensile strength and fracture strain that can be extracted from the loading curves. Table 3 lists the ultimate tensile strength of M0-7 models of sI methane hydrate with different defects of water vacancy, which are predicted by TIP4P, TIP4P/2005, TIP4P/ICE and TIP4P/EW water forcefields. Similar to previous studies (Shi et al., 2018), there is an apparent effect of the water model on the tensile mechanical properties such as ultimate tensile strength of defect-free sI clathrate hydrates (M0). Using TIP4P, TIP4P/2005, TIP4P/ICE and TIP4P/EW water models, the tensile strength of defect-free sI methane hydrate is predicted to be around 0.826, 1.135, 1.135 and 0.872 GPa, respectively. The tensile strength of perfect sI methane hydrates predicted by TIP4P, TIP4P/2005, TIP4P/ICE water models are in good agreement with previous data by Shi et al. (2018) and Xin et al. (2021).

With regard to sI methane hydrates containing defect of water vacancy, it is found from Table 3 that tensile strength obviously varies with the location and concentration of water vacancy defect, as well as the applied water forcefield. For hydrate sample with one water vacancy defect, it is identified that the tensile strength of M1 model predicted by TIP4P, TIP4P/2005 and TIP4P/ICE water forcefields is larger than that of M2 and 3 models, indicating that Type II and III defects play more important role in affecting the mechanical strength of sI methane hydrates than Type I defect. When predicting by TIP4P/EW water forcefield, however, sI methane hydrates with Type III defect is more mechanically robust than that with Types I and II defects in terms of tensile strength. It can be seen from Table 3 that TIP4P/ICE model predicts obviously higher tensile strength than other water models. This is because the absolute charges of oxygen and hydrogen atoms in TIP4P/ICE water model are larger than those of other three water models, resulting in stronger coulombic interactions.

As for the hydrate sample with defects of two water vacancies, the tensile strength is uniquely determined by the combination of two type defects and the applied water forcefield. For TIP4P/ICE and TIP4P/EW water forcefields, the M5 model of hydrate sample exhibits larger tensile strength than M4 and 6 models, suggesting that hydrate sample containing water vacancy defects of Type I and III is more mechanically stable structure that contains other combinations of two type defects. Whereas for the cases predicted by TIP4P and TIP4P/2005 water forcefields, the M4 and 6 models of hydrate samples show the largest tensile strength in the hydrate samples with a combination of two types of defects, respectively. Concerning the hydrate sample containing the three types of defects of water vacancy, the mechanical strength is also determined by the utilized water forcefield. In terms of the values of tensile strength, it is sorted as TIP4P/ICE >TIP4P/2005 >TIP4P/EW >TIP4P. Such sorting is also found for hydrate samples with defects of one and two-type water vacancies. Moreover, it is noted that, for the same category of model containing multi-defects, spatial distribution of water vacancy defects has impact on the mechanical properties such as tensile strength.

By comparison, the tensile strengths of defective hydrate samples predicted by the TIP4P, TIP4P/2005 and TIP4P/ICE water forcefields are lower than that of defect-free hydrate samples. This indicates that the presence of defects of water vacancy degrades the mechanical strength of sI methane hydrates. When predicting with TIP4P/EW water forcefield, however, it is observed that tensile strengths of M1-3, 5 and 7 models of hydrate samples are higher than that of the defect-free sample. This indicates that sI methane hydrates can be abnormally enhanced by the introduction of specific defects of water vacancy.

More intriguingly, with increasing the density of defects of water vacancy, there is no clear reduction in the tensile strength of defective hydrate samples predicted by those four water forcefields. For example, using TIP4P water forcefield, the M7 model of hydrate sample containing three water vacancies exhibits higher tensile strength than the M2 model

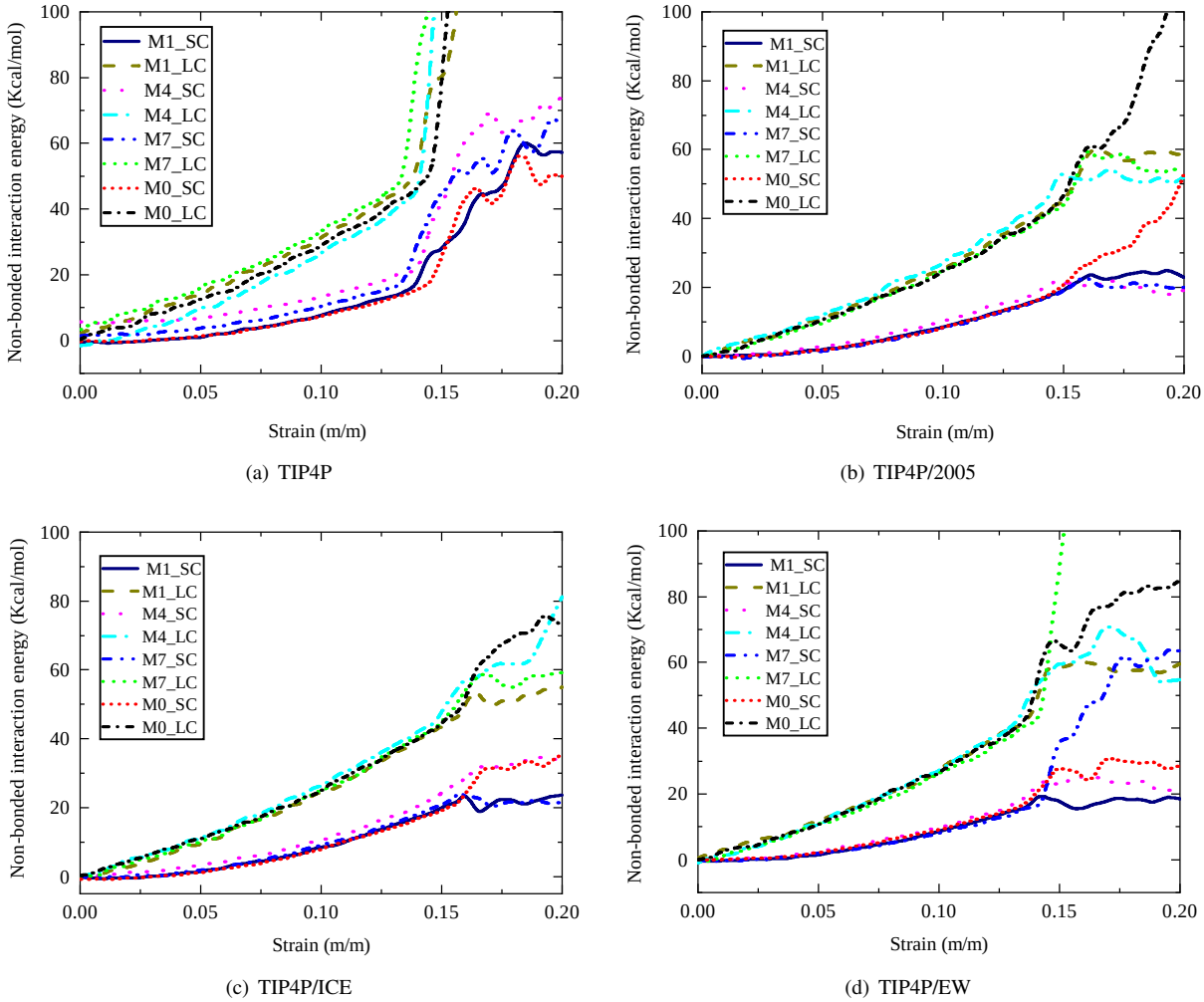

Fig. 4. Non-bonded interaction energy (ΔE) between water and methane molecules residing in the small 5^{12} cages (SC) and large $5^{12}6^2$ cages (LC) with strain for M0, 1, 4 and 7 models predicted by the four popular water models.

that contains one water vacancy defect. Using TIP4P/2005 water forcefield, the tensile strength of the M7 model is higher than that of M2, 4-6 models. By TIP4P/ICE water forcefield, M7 model shows higher tensile strength than M4-6 models that contain two water vacancies. Utilizing TIP4P/EW water forcefield, the tensile strength of the M7 model exceeds that of the M1, 4 and 6 models.

3.4 Non-bonded energetics between methane and clathrate cages

As is known, beyond HB interactions between water molecules, non-bonding interactions between guest and host molecules are also of crucial role in thermodynamically stabilizing clathrate hydrates consisting of water and guest molecules. Figs. 4(a)-4(d) shows the changes of non-bonded interaction energy (ΔE) between water and methane molecules residing in the small 5^{12} cages (SC) and large $5^{12}6^2$ cages (LC) with strain for M0, 1, 4 and 7 models of hydrate samples predicted by TIP4P, TIP4P/2005, TIP4P/ICE and TIP4P/EW water models, respectively. Below critical (failure) strains, ΔE of methane molecules and SC are monotonically increased with increasing uniaxial strain, and the increase in ΔE becomes more pronounced. This suggests that uniaxial global deformation reduces the non-bonded interactions of guest methane molecules with SC and LC, and their non-bonded interactions become weaker with increasing uniaxial strain. However, there exist significant differences in the ΔE between SC and LC for all water models with increasing uniaxial strain. For example, increase in the ΔE for methane and SC is less than that for methane and LC during the elastic straining, indicating that methane@SC are less deformed than methane@SL for at given global strains. Remarkably, there is a negligible difference in the ΔE for M0, 1, 4 and 7 models of hydrate samples. Surpassing the failure strains, ΔE can be enlarged or declined, depending on the adopted water model and the type of hydrate sample, indicating their distinct failure patterns.

3.5 Sphericity of clathrate cages

To quantitatively characterize the clathrate cage deformations of hydrate samples under mechanical load, the sphericity

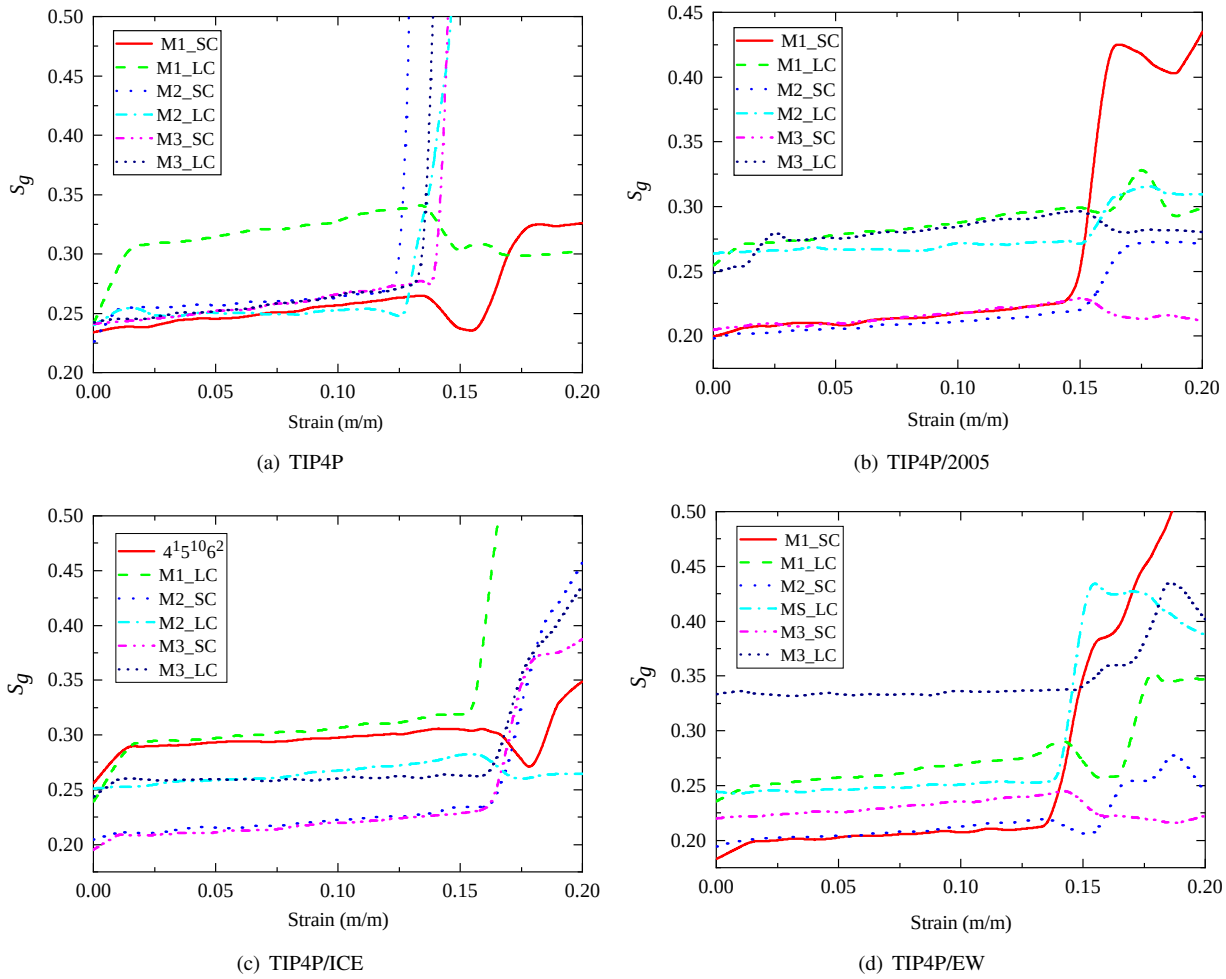

Fig. 5. The sphericity of the M1-3 models as a function of the tensile strain by calculating different water forcefields. The small 5^{12} cages (SC) are closer to a spherical shape.

of defective clathrate cages is introduced. In this study, the sphericity of clathrate cages (Sg) is on the basis of the radius of gyration (Kalashnikova and Sokolik, 2004; Moore and Molinero, 2009; Reinhardt and Doye, 2012) and is computed as follows

$$S_g = \frac{R_g}{1.5c^{1/3}} - 1 \tag{3}$$

with

$$R_g^2 = \frac{1}{c^2}\sum_{i>j}^{c}(r_i - r_j)^2 \tag{4}$$

where c is the number of water molecules in the defective clathrate cages, and here for the 5^{12} and $5^{12}6^2$ clathrate cages, c = 19 and 23, respectively. r_i and r_j are coordinates of oxygen atoms of water molecules in a clathrate cage. $1.5c^{1/3}$ reflects the approximate radius of gyration of perfect clathrate cages. For an ideal sphere, S_g = 0. Figs. 5(a)-5(d) shows the variations in the S_g of 5^{12} and $5^{12}6^2$ clathrate cages with one water vacancy with uniaxial strain predicted by TIP4P, TIP4P/2005, TIP4P/ICE and TIP4P/EW water models, respectively. Here, the M1, M2, and M3 models are selected to examine the effects of defect types on the sphericity of the 5^{12} and $5^{12}6^2$ clathrate cages.

At equilibrium state (zero strain), S_g of 5^{12} and $5^{12}6^2$ cages with one water vacancy varies from around 0.16-0.27, depending on the applied water forcefield and defect type of water vacancy. Such finite values of S_g result from that defective 5^{12} and $5^{12}6^2$ cages composed of polygonal rings are not spherical. Using TIP4P water forcefield, there is a negligible difference in the Sg between defective 5^{12} and $5^{12}6^2$ cages, as well as between 5^{12}/$5^{12}6^2$ cages with different types of water vacancy defects. Whereas by TIP4P/2005, TIP4P/ICE and TIP4P/EW water models, there are significant differences in the S_g. For example, the values of the S_g of defective 5^{12} and $5^{12}6^2$ cages predicted by TIP4P/2005 water forcefield are around 0.20 and 0.25, respectively. As for TIP4P/EW water forcefield, defective 5^{12}/$5^{12}6^2$ cages of M1, 2 and 3 models show S_g of around 0.16/0.23, 0.19/0.24 and 0.22/0.33, respectively. Upon tension, all defective clathrate cages show an increasing tendency in the S_g with increasing strain before critical (failure) strains, indicating that they are deformed during the stretching process. Based on the characteristics of the curves, the changes of S_g of defective 5^{12} and $5^{12}6^2$ cages

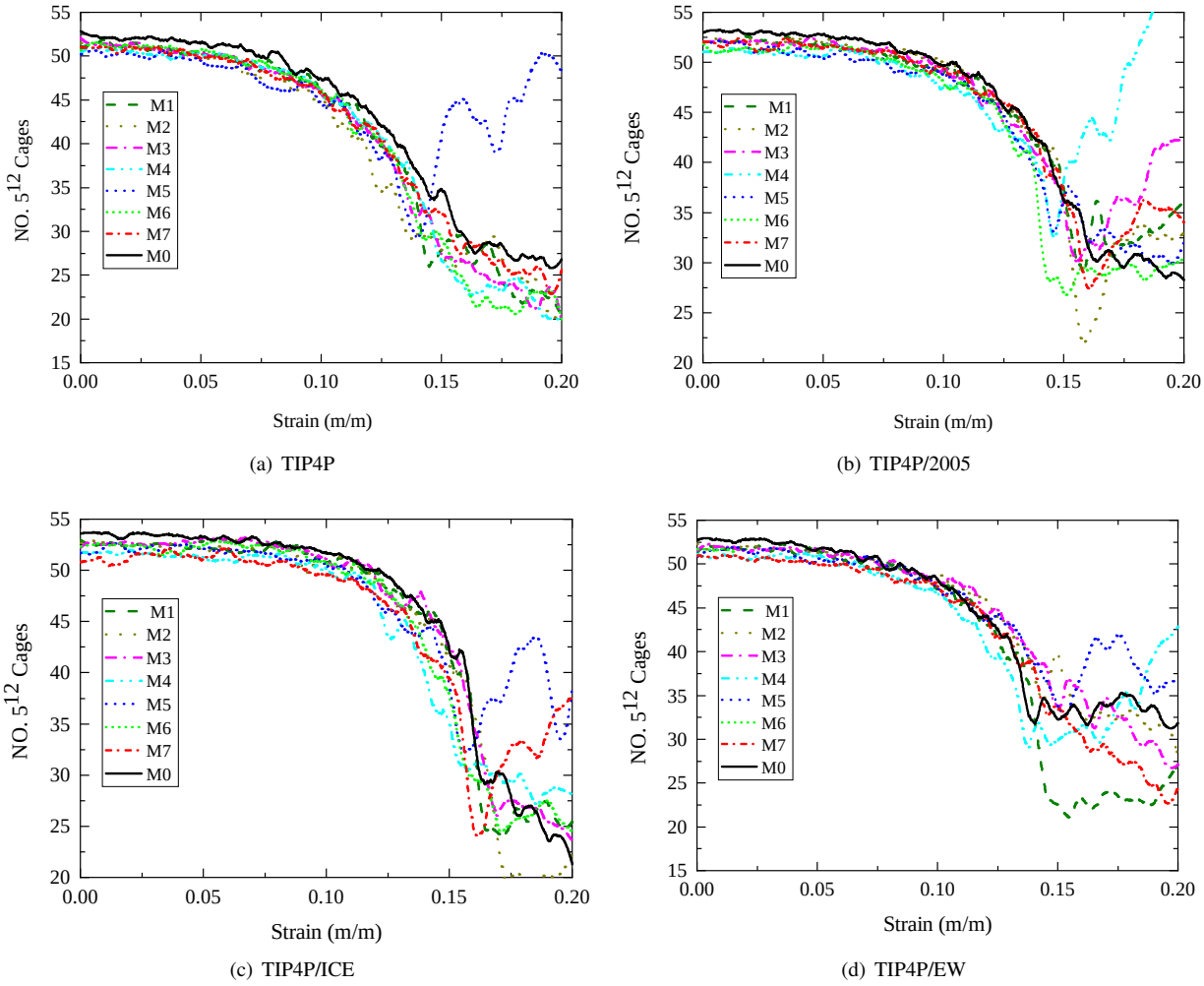

Fig. 6. The variations of 5^{12} cages for M0-7 models as subjected to uniaxial strain predicted by the four popular water models.

can be roughly divided into three different stages. In stage I that corresponds to strain of around 0.00-0.02, the values of S_g of defective 5^{12} and $5^{12}6^2$ cages increase significantly, indicating that the defective cages experience significant structural transformations in this loading stage. In stage II, the values of S_g of defective 5^{12} and $5^{12}6^2$ cages are enlarged at a slow rate. This is mainly because the defective cages are structural stable configurations past the first loading stage, and subjected to uniaxial strain at stage II, as-formed stable configurations formed from defective cages are almost elastically deformed. In the final stage, the S_g is dramatically changed, indicative that as-formed stable configurations are plastically deformed, resulting in their dissociations of clathrate configurations.

3.6 Dynamics of clathrate cages

Clathrate hydrates are mainly composed of water cages that encapsulate guest molecules. Subject to mechanical loads, the dynamic information of water cages is a good indicator of the structural stability of clathrate hydrates. Here, the information of water cages is extracted to reveal microstructural responses in methane hydrates. Figs. 6(a)-6(d) and 7(a)-7(d) show the variations in the number of 5^{12} and $5^{12}6^2$ clathrate cages of M0-7 models subjected to uniaxial strain predicted by TIP4P, TIP4P/2005, TIP4P /ICE and TIP4P/EW water models, respectively. As illustrated in Figs. 6 and 7, the numbers of both 5^{12} and $5^{12}6^2$ clathrate cages nonlinearly change with uniaxial strain. The reduction trend in the number of clathrate cages becomes more pronounced with an increasing strain before failure for all water models, indicating that dissociation of clathrate cages in hydrate systems can be caused by mechanical load. By comparison, upon strain before critical strains, defect-free methane hydrate has a larger number of cages than defective ones (with water vacancy), resulting from the fact that four cages in methane hydrate share one water molecule. Beyond the failure strains, however, an interesting phenomenon is that the number of clathrate cages can be further reduced or increased, depending on the adopted water forcefield, hydrate model and type of clathrate cage. For example, by TIP4P, TIP4P/ICE, and TIP4P/EW water forcefields, the number of 5^{12} cages of the M5 model is increased past the failure strain. In contrast, by excluding the M5 model, using TIP4P water forcefield, the number of 5^{12} cages in the M0-7 models is monotonically reduced beyond the failure strain. With regard to the case of the $5^{12}6^2$ cages, all adopted water

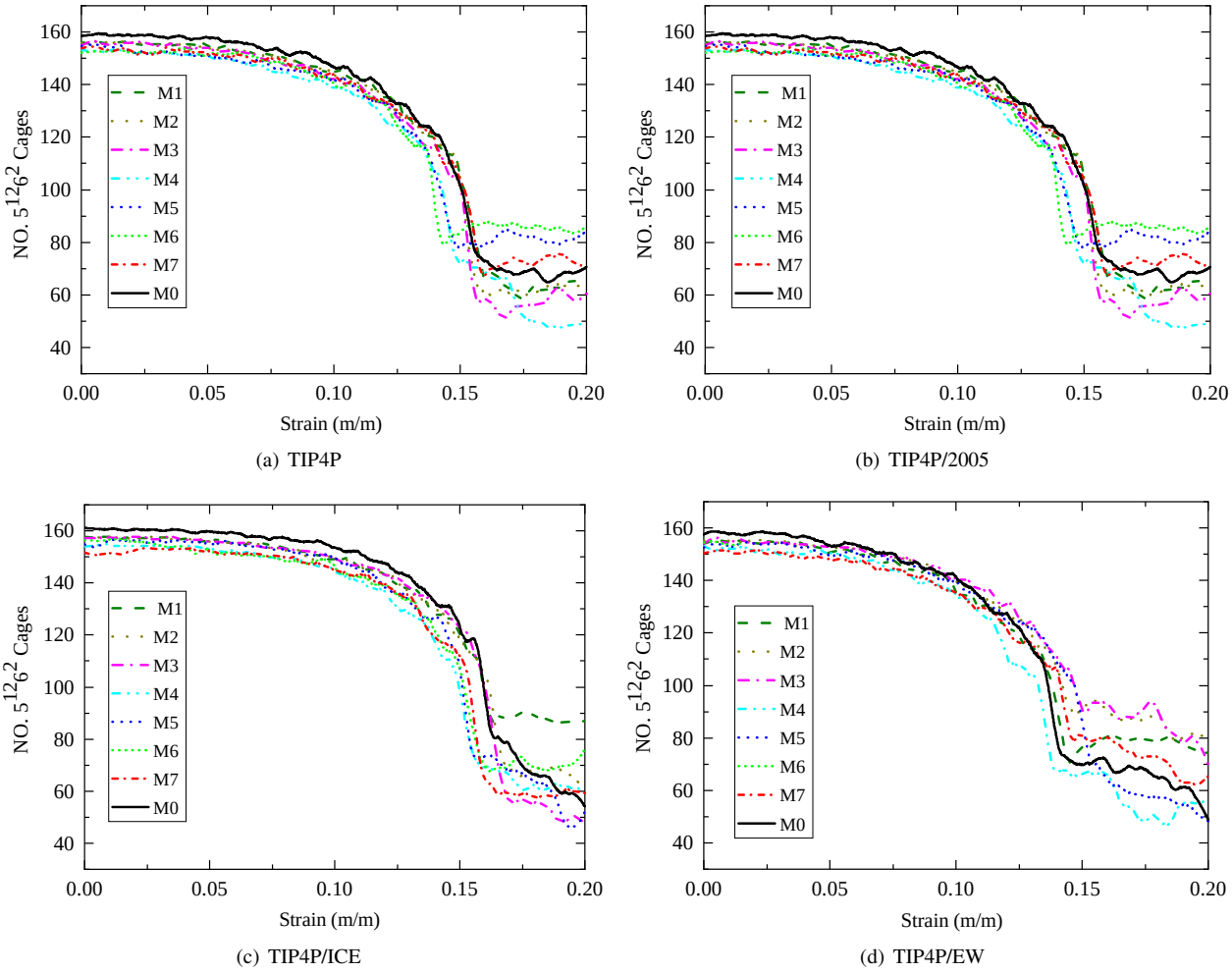

Fig. 7. The variations of $5^{12}6^2$ cages for M0-7 models as subjected to uniaxial strain predicted by the four popular water models.

models predict that the number of $5^{12}6^2$ cages in the M0-7 models of hydrate systems is further reduced or remains constant surpassing the failure strain. Such distinct changes in the number of clathrate cages past the failure strain indicate distinct plastic deformation mechanisms.

To further explore the microstructural responses and possible structural transformations of hydrate samples during the mechanical loading process, other types of clathrate cages besides conventional 5^{12} and $5^{12}6^2$ are identified. Fig. 8 shows the changes in the number of various types of clathrate cages in defective sI methane hydrate systems with strain varying from 0.10-0.20 predicted by TIP4P/ICE. The M0, M1, M4, and M7 models are representatively selected to analyze the formation of new cages. Note that other three water forcefields also predict formation of new cages in defective sI methane hydrates under straining, whereas for defect-free sI methane hydrates, new cages are seldom recognized during the stretching process. As is indicated in Fig. 8, a variety of unconventional $5^{12}6^3$, $5^{12}6^4$, $5^{12}6^5$, $5^{12}6^6$, $5^{12}6^8$, $4^15^{10}6^2$ clathrate cages form in the defective sI methane hydrate systems, and their numbers tend to increase with increasing strain. Moreover, the number of each type of newly formed cages is dictated by the type and density of water vacancy in the sI methane hydrate system, as well as the adopted water forcefield. For example, as for M0 model, the $4^15^{10}6^3$ cage forms more easily than other cages, whereas for M1 model, the $4^15^{10}6^2$ cage more readily occurs. With regard to M7 model that contains high density of water vacancy, there are a larger number and type of new cages, indicating that water vacancy in sI methane hydrate promotes the formation of new cages. Among the newly formed clathrate cages, the $4^15^{10}6^22$ cage is readily identified in all defective hydrate systems that are described by the four water forcefields. A previous study showed that water vacancy in hydrate systems can be dynamically transferred (Lo et al., 2017), while in this study, it is revealed that mechanical load could lead to the microstructural transformation of cages in sI methane hydrates.

3.7 Mechanical failure mechanisms

To understand the molecular insights into the strain-induced plastic deformation mechanisms in defective sI methane hydrates, the evolution of their molecular structures

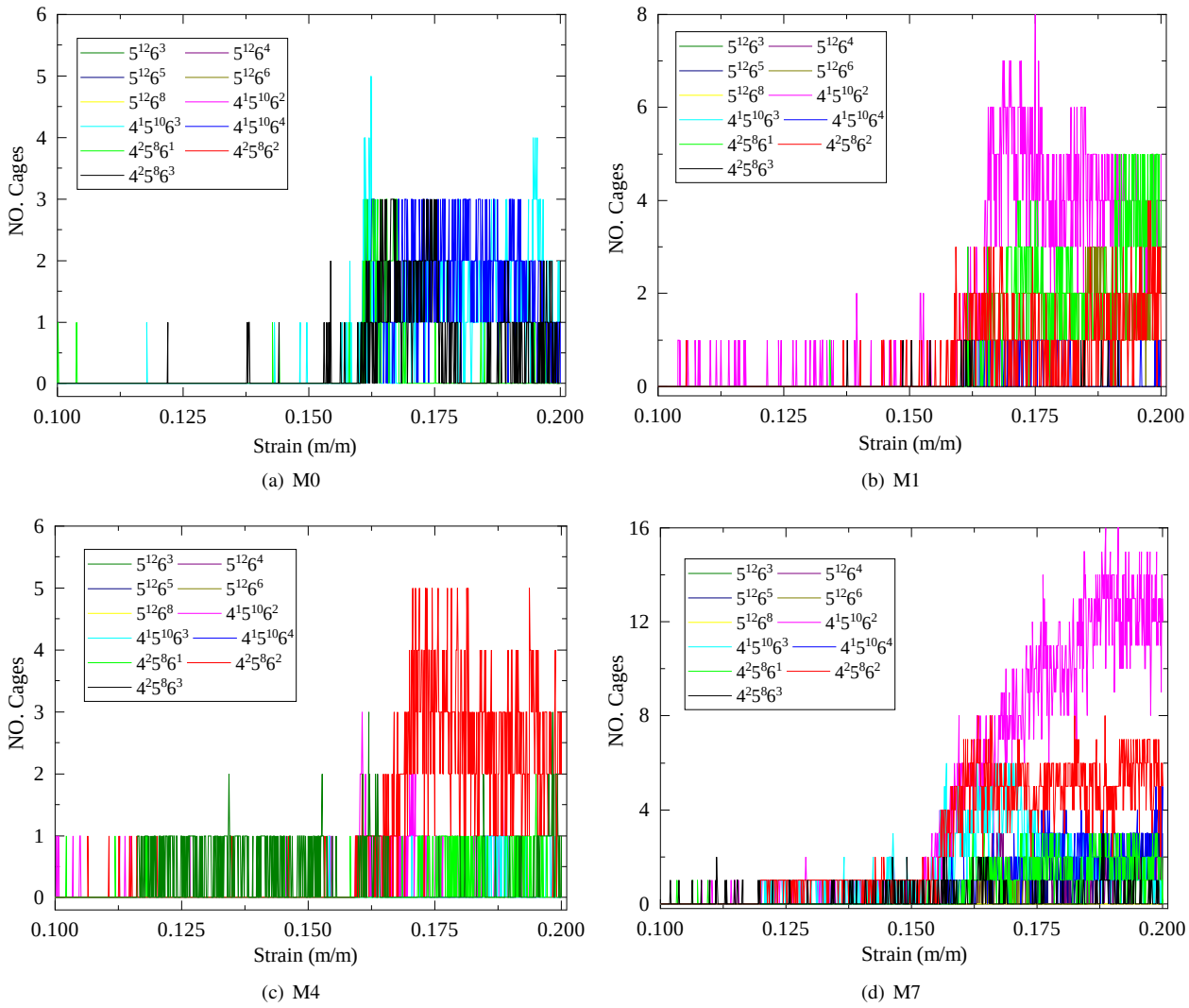

Fig. 8. The number of new cages for different models varies with the tensile strain (0.1-0.2) by using TIP4P/ICE water forcefield.

during the straining is recorded. Figs. 9(a) and 9(b) present a series of snapshots of the M4 and 7 models of defective hydrate crystals with TIP4P/ICE water forcefield at four critical strains, respectively, in which the color code is on the basis of the values of atomic shear strain. Note that the plastic deformation characteristics of all other tested samples predicted by the four different water models can be represented by Fig. 9. As is illustrated in Fig. 9(a), at the uniaxial strain of around 0.1590, there is an apparent high local shear strain in the vicinity of a water vacancy, and the region of high shear strain is rapidly enlarged with strain. At a strain of around 0.1594, the structures with high shear strains are destabilized via amorphization. With further augment of uniaxial strain, the hydrate sample is globally destabilized vis clear separation along the (001) crystallographic plane, explaining the sudden deep drop of loading stress in the curves of Fig. 3. The failure of hydrate crystal of M4 model is characterized by brittle fracture. However, there is another type of mechanical destabilization mechanism of defective hydrate crystal, for example, the M7 model. As is indicated by Fig. 9(b), at the uniaxial strain of around 0.1562, there are multiple local high shear strains. Followed by that, structures are locally destabilized via amorphization. With further increasing strain, local amorphizations propagate, resulting in structural collapse along the (001) crystallographic plane, which explains the sudden deep drop of loading stress in the tensile curves of Fig. 3. Interestingly, such collapse does not lead to the separation of hydrate samples that occurs in M4 model. Therefore, the failure of M7 model can be primarily characterized by ductile-like fracture.

To in-depth reveal the molecular insights into the deformational structural responses, the dynamics of clathrate cages of defective hydrates subjected to straining are captured. Fig. 10 shows a set of snapshots of the M4 and 7 models that correspond to those in Fig. 9, in which the color code is based on the types of clathrate cage. As is shown in Figs. 10(a)-10(b), as the failure locally occurs in M4 model, $4^1 5^{10} 6^2$ and $4^3 5^6 6^3$ cages are newly generated. As the failure propagates

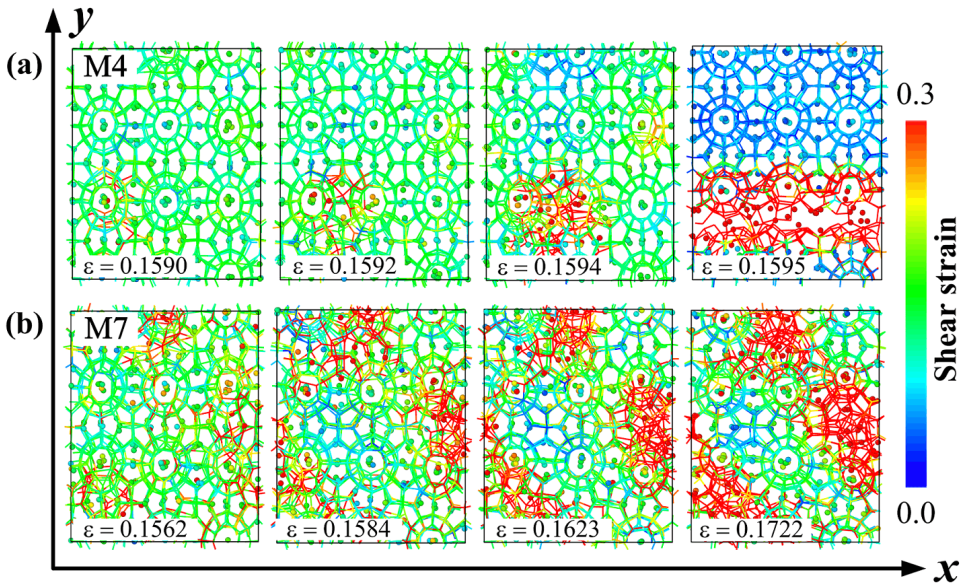

Fig. 9. The stress-induced fracture and defect-induced enhanced mechanisms in the hydrate systems predicted by the TIP4P/ICE water model. Side views of representative snapshots of the M4 and 7 models during the rupture process. The color code is based on shear strain.

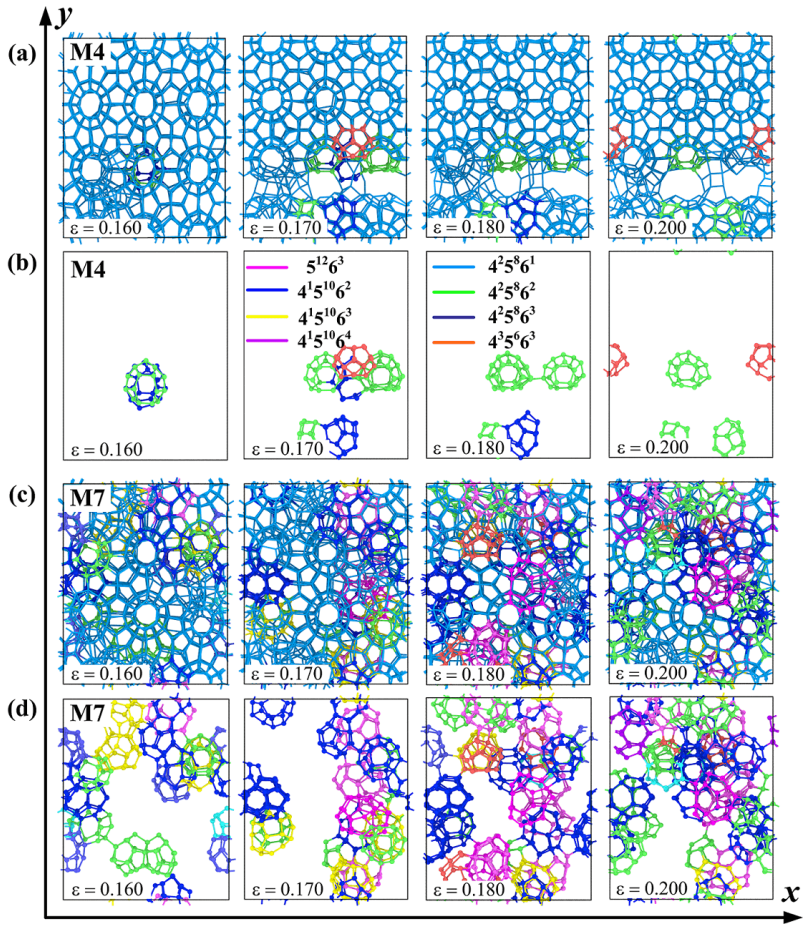

Fig. 10. The phase transition mechanisms in the hydrate systems predicted by the TIP4P/ICE water model. Side views of representative snapshots of the M4 and 7 models during the tension process. The color codes are based on the types of clathrate cage.

with increasing strain, there is an increase in the number and type of newly formed cages that mainly occurs in the vicinity of fracture location. For the M7 model under large strains, however, newly formed clathrate cages are well distributed in the hydrate systems, as shown in Figs. 10(c)-10(d). Moreover, the number of new cages and the number of types of new cages are much larger than the M4 model, In comparison with Fig. 9(b), it is identified that the newly formed cages mainly occur in the regions with higher shear strain. Such large number of newly formed cages occurred in the region of defects enable to experience large loading stress and strain, thereby enhancing the tensile strength. This explains the fact that sI methane hydrates containing unique defects of water vacancies show robust stress responses in Fig. 3. With further increasing strain, a large number of unconventional clathrate cages form, and the structures are dominated by unconventional clathrate cages but not by 5^{12} and $5^{12}6^2$ cages, resulting in the formation of amorphous methane hydrates.

4. Conclusions

In summary, the role of water vacancy defects on the mechanical stability of sI methane hydrates are investigated using classic MD simulations with four different water forcefields. Results show that the formation energy of water vacancy depends on the type of water vacancy, and is smaller than that in hexagonal water ice. The lattice constant of sI methane hydrates depends on the utilized water forcefields, the type and density of water vacancy. In mechanics, the stress responses are greatly dictated by the type and density of water vacancy, as well as the adopted water forcefield. Interestingly, the tensile strength of sI methane hydrates can be enhanced or reduced by water vacancy, originating from distinct microstructural transformations in the defective regions, for example, defect-induced enhancement mechanism is revealed by the formation of unconventional cages such as $5^{12}6^4$, $5^{12}6^5$, $4^15^{10}6^3$, $4^25^86^2$ and $4^15^{10}6^2$ cages at the weak locations, of which the $4^15^{10}6^2$ cages dominates Additionally, analysis of sphericity of clathrate cages reveal that 5^{12} cage is more difficult in geometrical distortion than $5^{12}6^2$ one during the stretching. This study highlights the role of defect of water vacancies on the stability of methane hydrates that is helpful in the important applications of clathrate hydrates.

Acknowledgement

This work is financially supported by the National Natural Science Foundation of China (Grant Nos. 11772278, 12172314, 12002350 and 11904300), the Jiangxi Provincial Outstanding Young Talents Program (Grant No. 20192BCBL23029), the Fundamental Research Funds for the Central Universities (Xiamen University: Grant No. 20720210025). Y. Yu and Z. Xu from the Information and Network Center of Xiamen University for help with the high-performance computer.

Conflict of interest

The authors declare no competing interest.

References

Abascal, J. L. F., Vega, C. A general purpose model for the condensed phases of water: TIP4P/2005. Journal of Chemical Physics, 2005, 123(23): 234505.

Atig, D., Broseta, D., Pereira, J. M., et al. Contactless probing of polycrystalline methane hydrate at pore scale suggests weaker tensile properties than thought. Nature Communications, 2020, 11(1): 3379.

Cai, S., Tang, Q., Tian, S., et al. Molecular simulation study on the microscopic structure and mechanical property of defect-containing sI methane hydrate. International Journal of Molecular Sciences, 2019, 20(9): 2305.

Cao, P., Ning, F., Wu, J., et al. Mechanical response of nanocrystalline ice-contained methane hydrates: Key role of water ice. ACS Applied Materials & Interfaces, 2020, 12(12): 14016-14028.

Cao, P., Sheng, J., Wu, J., et al. Mechanical creep instability of nanocrystalline methane hydrates. Physical Chemistry Chemical Physics, 2021, 23(5): 3615-3626.

Cao, P., Wu, J., Zhang, Z., et al. Mechanical properties of methane hydrate: Intrinsic differences from ice. Journal of Physical Chemistry C, 2018, 122(51): 29081-29093.

Casco, M. E., Silvestre-Albero, J., Ramirez-Cuesta, A. J., et al. Methane hydrate formation in confined nanospace can surpass nature. Nature Communications, 2015, 6(1): 6432.

Chen, J., Wang, Y. H., Lang, X. M., et al. Energy-efficient methods for production methane from natural gas hydrates. Journal of Energy Chemistry, 2015, 24(5): 552-558.

Chong, Z. R., Yang, S. H. B., Babu, P., et al. Review of natural gas hydrates as an energy resource: Prospects and challenges. Applied Energy, 2016, 162: 1633-1652.

Costandy, J., Michalis, V. K., Tsimpanogiannis I. N., et al. Molecular dynamics simulations of pure methane and carbon dioxide hydrates: Lattice constants and derivative properties. Molecular Physics, 2016, 114(18): 2672-2687.

de Koning, M., Antonelli, A., da Silva, A. J. R., et al. Structure and energetics of molecular point defects in ice I_h. Physical Review Letters, 2006, 97(15): 155501.

Everett, S. M., Rawn, C. J., Chakoumakos, B. C., et al. Insights into the structure of mixed CO_2/CH_4 in gas hydrates. American Mineralogist, 2015, 100(5-6): 1203-1208.

Everett, S. M., Rawn, C. J., Keffer, D. J., et al. Kinetics of methane hydrate decomposition studied via in situ low temperature X-ray powder diffraction. Journal of Physical Chemistry A, 2013, 117(17): 3593-3598.

Fan, S., Wang, X., Wang, Y., et al. Recovering methane from quartz sand-bearing hydrate with gaseous CO_2. Journal of Energy Chemistry, 2017, 26(4): 655-659.

Graves, C. A., James, R. H., Sapart, C. J., et al. Methane in shallow subsurface sediments at the landward limit of

the gas hydrate stability zone offshore western Svalbard. Geochimica et Cosmochimica Acta, 2017, 198: 419-438.

Hansen, T. C., Falenty, A., Kuhs, W. F. Lattice constants and expansivities of gas hydrates from 10 K up to the stability limit. Journal of Chemical Physics, 2016, 144(5): 054301.

Jacobson, L. C., Molinero, V. A methane-water model for coarse-grained simulations of solutions and clathrate hydrates. Journal of Physical Chemistry B, 2010, 114(21): 7302-7311.

Jendi, Z. M., Servio, P., Rey, A. D. Ideal strength of methane hydrate and ice I_h from first-principles. Crystal Growth & Design, 2015, 15(11): 5301-5309.

Jorgensen, W. L., Maxwell, D. S., TiradoRives, J. Development and testing of the OPLS all-atom force field on conformational energetics and properties of organic liquids. Journal of the American Chemical Society, 1996, 118(45): 11225-11236.

Kalashnikova, O. V., Sokolik, I. N. Modeling the radiative properties of nonspherical soil-derived mineral aerosols. Journal of Quantitative Spectroscopy and Radiative Transfer, 2004, 87(2): 137-166.

Kaminski, G., Duffy, E. M., Matsui, T., et al. Free-energies of hydration and pure liquid properties of hydrocarbons from the OPLS all-atom model. Journal of Physical Chemistry, 1994, 98(49): 13077-13082.

Koh, C. A., Sloan, E. D. Natural gas hydrates: Recent advances and challenges in energy and environmental applications. AIChE Journal, 2007, 53(7): 1636-1643.

Lee, Y.-L., Kleis, J., Rossmeisl, J., et al. Ab initioenergetics of $LaBO_3$(001) (B = Mn, Fe, Co, and Ni) for solid oxide fuel cell cathodes. Physical Review B, 2009, 80(22): 224101.

Liang, S., Liang, D., Wu, N., et al. Molecular mechanisms of gas diffusion in CO_2 hydrates. The Journal of Physical Chemistry C, 2016, 120(30): 16298-16304.

Liang, S., Liang, D., Wu, N., et al. Transient translational and rotational water defects in gas hydrates. Journal of Physical Chemistry C, 2017, 121(33): 17595-17602.

Liu, W., Zhao, J., Luo, Y., et al. Experimental measurements of mechanical properties of carbon dioxide hydrate-bearing sediments. Marine and Petroleum Geology, 2013, 46: 201-209.

Lo, H., Lee, M. T., Lin, S. T. Water vacancy driven diffusion in clathrate hydrates: Molecular dynamics simulation study. Journal of Physical Chemistry C, 2017, 121(15): 8280-8289.

Luff, R., Wallmann, K. Fluid flow, methane fluxes, carbonate precipitation and biogeochemical turnover in gas hydrate-bearing sediments at hydrate ridge, cascadia margin: Numerical modeling and mass balances. Geochimica et Cosmochimica Acta, 2003, 67(18): 3403-3421.

Mayeshiba, T., Morgan, D. Strain effects on oxygen vacancy formation energy in perovskites. Solid State Ionics, 2017, 311: 105-117.

McMullan, R. K., Jeffrey, G. A. Polyhedral clathrate hydrates. IX. structure of ethylene oxide hydrate. The Journal of Chemical Physics, 1965, 42(8): 2725-2732.

Moore, E. B., Molinero, V. Growing correlation length in supercooled water. The Journal of Chemical Physics, 2009, 130(24): 244505.

Ning, F. L., Yu, Y. B., Kjelstrup, S., et al. Mechanical properties of clathrate hydrates: Status and perspectives. Energy & Environmental Science, 2012, 5(5): 6779-6795.

Ogienko, A. G., Kurnosov, A. V., Manakov, A. Y., et al. Gas hydrates of argon and methane synthesized at high pressures: Composition, thermal expansion, and self-preservation. Journal of Physical Chemistry B, 2006, 110(6): 2840-2846.

Plimpton, S. Fast parallel algorithms for short-range molecular-dynamics. Journal of Computational Physics, 1995, 117(1): 1-19.

Reinhardt, A., Doye, J. P. K. Free energy landscapes for homogeneous nucleation of ice for a monatomic water model. Journal of Chemical Physics, 2012, 136(5): 054501.

Rempel, A. W., Buffett, B. A. Formation and accumulation of gas hydrate in porous media. Journal of Geophysical Research: Solid Earth, 1997, 102(B5): 10151-10164.

Román-Peréz, G., Moaied, M., Soler, J. M., et al. Stability, adsorption, and diffusion of CH_4, CO_2, and H_2 in clathrate hydrates. Physical Review Letters, 2010, 105(14): 145901.

Shaibu, R., Sambo, C., Guo, B., et al. An assessment of methane gas production from natural gas hydrates: Challenges, technology and market outlook. Advances in Geo-Energy Research, 2021, 5(3): 318-332.

Shi, Q., Cao, P. Q., Han, Z., et al. Role of guest molecules in the mechanical properties of clathrate hydrates. Crystal Growth & Design 2018, 18(11): 6729-6741.

Shpakov, V. P., Tse, J. S., Tulk, C. A., et al. Elastic moduli calculation and instability in structure I methane clathrate hydrate. Chemical Physics Letters, 1998, 282(2): 107-114.

Sloan, E. D. Fundamental principles and applications of natural gas hydrates. Nature, 2003, 426(6964): 353-359.

Sveinsson, H. A., Ning, F., Cao, P., et al. Grain-size-governed shear failure mechanism of polycrystalline methane hydrates. Journal of Physical Chemistry C, 2021, 125(18): 10034-10042.

Uchida, T., Takeya, S., Chuvilin, E. M., et al. Decomposition of methane hydrates in sand, sandstone, clays, and glass beads. Journal of Geophysical Research: Solid Earth, 2004, 109(B5): B05206.

Udachin, K. A., Ratcliffe, C. I., Ripmeester, J. A. A dense and efficient clathrate hydrate structure with unusual cages. Angewandte Chemie-International Edition, 2001, 40(7): 1303-1305.

Vidal-Vidal, Á., Pérez-Rodríguez, M., Piñeiro, M. M. Direct transition mechanism for molecular diffusion in gas hydrates. RSC Advances, 2016, 6(3): 1966-1972.

Vidal-Vidal, Á., Pérez-Rodríguez, M., Torré, J. P., et al. DFT calculation of the potential energy landscape topology and Raman spectra of type I CH_4 and CO_2 hydrates. Physical Chemistry Chemical Physics, 2015, 17(10): 6963-6975.

Waite, W. F., Santamarina, J. C., Cortes, D. D., et al. Physical properties of hydrate-bearing sediments. Reviews of

Geophysics, 2009, 47(4): RG4003.

Walsh, M. R., Hancock, S. H., Wilson, S. J., et al. Preliminary report on the commercial viability of gas production from natural gas hydrates. Energy Economics, 2009, 31(5): 815-823.

Watkins, M., Pan, D., Wang, E. G., et al. Large variation of vacancy formation energies in the surface of crystalline ice. Nature Materials, 2011, 10(10): 794-798.

Wu, J., Ning, F., Trinh, T. T., et al. Mechanical instability of monocrystalline and polycrystalline methane hydrates. Nature Communications, 2015, 6(1): 8743.

Wu, J., Skallerud, B., He, J., et al. Grain-size induced strengthening and weakening of dislocation-free polycrystalline gas hydrates. Procedia IUTAM, 2017, 21: 11-16.

Xin, Y., Shi, Q., Xu, K., et al. Tensile properties of structural I clathrate hydrates: Role of guest-host hydrogen bonding ability. Frontiers of Physics, 2021, 16(3): 33504.

Xu, K., Yang, L., Liu, J., et al. Mechanical properties of CH_4-CO_2 heteroclathrate hydrates. Energy & Fuels, 2020, 34(11): 14368-14378.